

Journal Pre-proof

Retrieval of surface PM_{2.5} mass concentrations over North China using visibility measurements and GEOS-Chem simulations

Sixuan Li, Lulu Chen, Gang Huang, Jintai Lin, Yingying Yan, Ruijing Ni, Yanfeng Huo, Jingxu Wang, Mengyao Liu, Hongjian Weng, Yonghong Wang, Zifa Wang

PII: S1352-2310(19)30760-5

DOI: <https://doi.org/10.1016/j.atmosenv.2019.117121>

Reference: AEA 117121

To appear in: *Atmospheric Environment*

Received Date: 1 February 2019

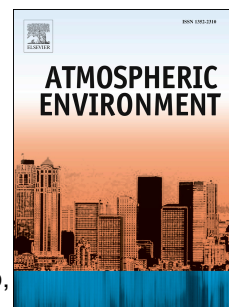
Revised Date: 4 November 2019

Accepted Date: 6 November 2019

Please cite this article as: Li, S., Chen, L., Huang, G., Lin, J., Yan, Y., Ni, R., Huo, Y., Wang, J., Liu, M., Weng, H., Wang, Y., Wang, Z., Retrieval of surface PM_{2.5} mass concentrations over North China using visibility measurements and GEOS-Chem simulations, *Atmospheric Environment* (2019), doi: <https://doi.org/10.1016/j.atmosenv.2019.117121>.

This is a PDF file of an article that has undergone enhancements after acceptance, such as the addition of a cover page and metadata, and formatting for readability, but it is not yet the definitive version of record. This version will undergo additional copyediting, typesetting and review before it is published in its final form, but we are providing this version to give early visibility of the article. Please note that, during the production process, errors may be discovered which could affect the content, and all legal disclaimers that apply to the journal pertain.

© 2019 Published by Elsevier Ltd.



1 **Retrieval of surface PM_{2.5} mass concentrations over North China using visibility**
2 **measurements and GEOS-Chem simulations**

3 Sixuan Li^{1,2}, Lulu Chen³, Gang Huang^{1,2,4,*}, Jintai Lin^{3,**}, Yingying Yan³, Ruijing Ni³,
4 Yanfeng Huo⁵, Jingxu Wang³, Mengyao Liu³, Hongjian Weng³, Yonghong Wang⁶, Zifa
5 Wang^{2,7}

6 ¹State Key Laboratory of Numerical Modeling for Atmospheric Sciences and
7 Geophysical Fluid Dynamics (LASG), Institute of Atmospheric Physics, Chinese
8 Academy of Sciences, Beijing 100029, China

9 ²University of Chinese Academy of Sciences, Beijing 100000, China

10 ³Laboratory for Climate and Ocean-Atmosphere Studies, Department of Atmospheric
11 and Oceanic Sciences, School of Physics, Peking University, Beijing 100871, China

12 ⁴Laboratory for Regional Oceanography and Numerical Modeling, Qingdao National
13 Laboratory for Marine Science and Technology, Qingdao 266237, China

14 ⁵Anhui Institute of Meteorological Sciences, Hefei 230031, China

15 ⁶Institute for Atmospheric and Earth System Research / Physics, Faculty of Science,
16 P.O. Box 64, 00014 University of Helsinki, Helsinki, Finland

17 ⁷State Key Laboratory of Atmospheric Boundary Layer Physics and Atmospheric
18 Chemistry, Institute of Atmospheric Physics, Chinese Academy of Sciences, Beijing
19 100000, China

20

21 Submitted to: Atmospheric Environment

22

23 Corresponding author.

24 E-mail address: hg@mail.iap.ac.cn (G. Huang). linjt@pku.edu.cn (J.-T. Lin).

25 Highlights

- 26 • We integrate visibility data and GEOS-Chem simulations to estimate $PM_{2.5}$
27 concentrations in 2014 over North China.
- 28 • Visibility converted $PM_{2.5}$ are spatiotemporally consistent with $PM_{2.5}$
29 measurements.
- 30 • Our method provides a novel, plausible way to retrieve long-term variation of
31 $PM_{2.5}$.

32

33

34

35

36

37

38

39

40

41

42

43

44

45

46 **Abstract**

47 Despite much effort made in studying human health associated with fine particulate
48 matter (PM_{2.5}), our knowledge about PM_{2.5} and human health from a long-term
49 perspective is still limited by inadequately long data. Here, we presented a novel
50 method to retrieve surface PM_{2.5} mass concentrations using surface visibility
51 measurements and GEOS-Chem model simulations. First, we used visibility
52 measurements and the ratio of PM_{2.5} and aerosol extinction coefficient (AEC) in
53 GEOS-Chem to calculate visibility-inferred PM_{2.5} at individual stations (SC-PM_{2.5}).
54 Then we merged SC-PM_{2.5} with the spatial pattern of GEOS-Chem modeled PM_{2.5} to
55 obtain a gridded PM_{2.5} dataset (GC-PM_{2.5}). We validated the GC-PM_{2.5} data over the
56 North China Plain on a 0.3125° longitude x 0.25° latitude grid in January, April, July
57 and October 2014, using ground-based PM_{2.5} measurements. The spatial patterns of
58 temporally averaged PM_{2.5} mass concentrations are consistent between GC-PM_{2.5} and
59 measured data with a correlation coefficient of 0.79 and a linear regression slope of
60 0.80. The spatial average GC-PM_{2.5} data reproduce the day-to-day variation of observed
61 PM_{2.5} concentrations with a correlation coefficient of 0.96 and a slope of 1.0. The
62 mean bias is less than 12 µg/m³ (< 14%). Future research will validate the proposed
63 method using multi-year data, for purpose of studying long-term PM_{2.5} variations and
64 their health impacts since 1980.

65

66 **Keywords:** Visibility; Chemical Transport Model (CTM); PM_{2.5}; Spatial pattern; Time
67 series; North China Plain (NCP).

68

69 **1. Introduction**

70 Particulate matter with diameter less than 2.5 µm (PM_{2.5}) affects the climate,
71 visibility and human health (Lelieveld et al., 2015; Allen et al., 2014; Wang et al., 2015).

72 According to a Global Burden of Disease study (Lim et al., 2012), global PM_{2.5}
73 pollution accounted for 3.1 million deaths in 2010, predominantly in China and India.
74 A recent study revealed that transboundary PM_{2.5} pollution associated with
75 international trade and atmospheric transport together caused 0.76 million premature
76 deaths worldwide in 2007 (Zhang et al., 2017). Studies on fine particle matter health
77 impacts and climate influences require historical PM_{2.5} data. Therefore, to fully assess
78 the health impacts of PM_{2.5}, it is crucial to get access to long-term PM_{2.5} data across
79 multiple decades. However, to our knowledge, long-term PM_{2.5} data are lacking
80 especially in developing countries.

81 Surface PM_{2.5} mass concentrations in China are measured typically by either
82 Tapered Element Oscillating Microbalances (TEOM) or BETA-ray instruments. In
83 China, continuous PM_{2.5} measurements are sparse before 2013. The Chinese official air
84 quality monitoring network measures PM_{2.5} and other pollutants since 2013, mostly in
85 the urban areas. These data form the basis for many recent studies on the spatial and
86 temporal characteristics of urban air pollution and their causes over China (Liu et al.,
87 2018; Wang et al., 2014; Ge et al., 2018). However, these measurement data cannot be
88 used to analyze long-term trends and variability of PM_{2.5} and resulting health effects.
89 Therefore, alternative approaches to retrieving surface PM_{2.5} concentrations were
90 developed in the past decades.

91 Aerosol Optical Depth (AOD) data based on modern satellite remote sensing have
92 been used widely to retrieve surface PM_{2.5} concentrations due to their good spatial
93 coverage. AOD data are available from multiple satellite instruments, such as the
94 Moderate Resolution Imaging Spectroradiometer (MODIS, since 2000), the Multiangle
95 Imaging SpectroRadiometer (MISR, since 2000), and the Sea-viewing Wide
96 Field-of-view Sensor (SeaWiFS, since 1998) (Liu et al., 2017). These AOD data have
97 been combined with chemical transport model simulations or statistical approaches to
98 derive surface PM_{2.5} (Boys et al., 2014; Geng et al., 2015; van Donkelaar et al., 2010;

99 van Donkelaar et al., 2015).

100 van Donkelaar et al. (2010) estimated the global distribution of $PM_{2.5}$ using
101 satellite MODIS and MISR AOD products and GEOS-Chem simulations from 2001 to
102 2006. Their estimated $PM_{2.5}$ values show good agreement with observed $PM_{2.5}$ over
103 North America. Using the same method and MODIS, MISR and SeaWiFS AOD data,
104 Boys et al. (2014) produced a 15-year time series (1998-2012) of surface $PM_{2.5}$
105 concentrations worldwide, which agreed well with the situ measurements in Eastern
106 U.S. van Donkelaar et al. (2015) used the Geographically Weighted Regression (GWR)
107 statistical model to improve the $PM_{2.5}$ inference from AOD and GEOS-Chem
108 simulations. Their analysis showed that local variability in surface elevation and urban
109 emissions are important sources of uncertainty in retrieving $PM_{2.5}$ concentrations.
110 Using satellite AOD data and high-resolution GEOS-Chem simulations, Geng et al.
111 (2015) estimated surface $PM_{2.5}$ concentrations over China during 2006-2012, after
112 using CALIOP aerosol vertical profile data to correct for model biases. They found
113 very good spatial agreement between satellite-derived and measured $PM_{2.5}$
114 concentrations.

115 However, there are a number of limitations embedded in such satellite-based
116 $PM_{2.5}$ inference approaches. Model simulations are subject to errors in the model
117 representations of atmospheric processes, especially the vertical mixing and transport
118 that directly affect the simulated aerosol vertical profiles (Lin and McElroy, 2010; Liu
119 et al., 2018). Satellite-based AOD datasets are subject to a large number of missing
120 values due to screening for cloudy and strongly surface reflecting scenes. The AOD
121 datasets may have a low sampling bias, because high aerosol scenes may be mis-treated
122 as cloudy ones and screened out (Lin and Li, 2016). In addition, there are no reliable
123 satellite AOD data over land before 1998.

124 Satellite AOD data can also be combined with statistical models or machine
125 learning approaches to infer surface $PM_{2.5}$ concentrations. Taking meteorology and

126 land use information into model, Ma et al. (2014) estimated surface $PM_{2.5}$
127 concentrations using AOD from MODIS and MISR as a primary predictor. Zheng et al.
128 (2016) constructed linear mixed-effects models to convert MODIS AOD data and
129 other predictors to ground-level $PM_{2.5}$ concentrations over three major industrialized
130 regions in China. They corrected the predicted $PM_{2.5}$ concentrations by observed
131 $PM_{2.5}$. Li et al. (2017) applied a Geo-Intelligent Deep Learning approach to estimate
132 $PM_{2.5}$ over China, and they showed that in 2015 over 80% of Chinese lived in areas
133 with annual mean $PM_{2.5}$ concentrations above the WHO IT-1 standard levels (35
134 $\mu\text{g}/\text{m}^3$). Nonetheless, these statistical or machine learning approaches may have
135 difficulties in establishing/explaining the causality between $PM_{2.5}$ and predictors,
136 which poses the question of how the established relationships can be extrapolated to
137 other times and/or regions. The coefficient of determination (R^2) of such methods
138 declines substantially from 0.41-0.98 when the training dataset is used to 0.31-0.55
139 when the predictive dataset is used (Wei et al., 2019). In addition, satellite AOD data
140 have their own limitations, as mentioned above.

141 Visibility measurements available for multiple decades from ground
142 meteorological stations have also been used, together with statistical models, for $PM_{2.5}$
143 inference. Visibility represents horizontal light extinction, which is highly related with
144 the amount of $PM_{2.5}$, its chemical compositions, size distributions, optical properties,
145 and hygroscopicity (Charlson, 1969; Sinclair et al., 1974; Song et al., 2003). Visibility
146 and $PM_{2.5}$ concentrations are negatively correlated with a power law relationship (Zhao
147 et al., 2011; Zhang et al., 2019). Based on visibility data from 674 meteorological
148 monitoring sites and a statistical model, Liu et al. (2017) inferred the long-term
149 (1957-1964 and 1973-2014) changes of $PM_{2.5}$ pollution in China. They found $PM_{2.5}$
150 concentrations reached 60-80 $\mu\text{g}/\text{m}^3$ over the northern part of the North China Plain
151 during the 1950s-1960s, increasing to levels generally higher than 90 $\mu\text{g}/\text{m}^3$ since then.
152 Shen et al. (2016) retrieved historical (1979-2003) $PM_{2.5}$ mass concentrations in Xi'an
153 using visibility measurements and an exponential regression model, and they found

154 decreasing trends by $-4.6 \mu\text{g}/\text{m}^3/\text{year}$ and $-12.1 \mu\text{g}/\text{m}^3/\text{year}$ during 1979-1996 and
155 2007-2011, respectively, in contrast to a growth during 1997-2007 by $8.8 \mu\text{g}/\text{m}^3/\text{year}$.
156 However, statistical models are subject to abovementioned limitations.

157 This study presents a new method to retrieve surface $\text{PM}_{2.5}$ mass concentrations
158 using GEOS-Chem simulations and surface visibility measurements. The method is
159 inspired by our present study (Lin and Li, 2016; Lin et al., 2014) that used GEOS-Chem
160 and visibility data to infer AOD over East China, which showed high consistency with
161 AEROSOL ROBOTIC NETWORK (AERONET) and MODIS AOD data in terms of a low bias
162 and high temporal and spatial correlations. Here we proposed a similar method to
163 retrieve $\text{PM}_{2.5}$ concentrations over the NCP in January, April, July and October 2014
164 (i.e., covering four seasons). In particular, we used GEOS-Chem to help convert
165 visibility to $\text{PM}_{2.5}$ concentration at each site and then to a gridded space, in order to
166 facilitate further applications such as health impact analysis. We further validated the
167 retrieved $\text{PM}_{2.5}$ data against ground $\text{PM}_{2.5}$ measurements.

168 **2. Data and Methods**

169 **2.1 Surface $\text{PM}_{2.5}$ mass concentration measurements**

170 Hourly surface $\text{PM}_{2.5}$ concentration measurements were obtained from the China
171 National Environmental Monitoring Centre (CNEMC). The filled circles in Figure 1
172 show the 396 observation sites over the NCP used here. The sites are concentrated in
173 urban areas and lack coverage in rural and remote areas. Thus the observed data may
174 not fully represent the regional air quality.

175 At these 396 sites, $\text{PM}_{2.5}$ concentrations are measured by either TEOM or
176 Beta-attenuation instruments. Quality control is done through a fully automatic outlier
177 detection method for four types of outliers: temporal and spatial inconsistency, low
178 variance, periodic calibration exceptions, and PM_{10} concentrations being lower than
179 $\text{PM}_{2.5}$ concentrations (Wu et al., 2018). Additionally, we required that there are at least

180 20 hourly data for each day, 20 days per month, 2 months in January, April, July and
181 October 2014. We chose the four months to represent individual seasons, instead of
182 choosing all months, to reduce the computational costs of respective GEOS-Chem
183 simulations. When comparing with $PM_{2.5}$ measurements, we excluded data at times
184 when either visibility-converted $PM_{2.5}$ or measured $PM_{2.5}$ data were missing.

185 **2.2 Visibility and other meteorological data**

186 Visibility, temperature, wind speed and Relative Humidity (RH) measurements at
187 610 sites in January, April, July and October 2014 were obtained from Chinese
188 Meteorological Administration (CMA). The gray crosses in Figure 1 show the
189 meteorological sites.

190 For our study period, visibility is measured automatically by Forward Scattering
191 Visibility Meter (FSVM) which has a scattering angle of 30° – 50° . The instrument
192 ignores the absorption of light by the atmosphere, thus the derived scatter coefficient is
193 scaled up by an embedded algorithm to account for absorption and better represent the
194 total extinction coefficient before the value is converted to visibility (Tan et al., 2010).
195 Chinese meteorological stations mostly use the HY-V35 automatic visibility
196 instrument manufactured by Huayun Shengda Company, with core components of the
197 instrument purchased from Vaisala, Finland. HY-V35 passed the assessment of
198 various indicators of CMA on May 2011. The instrument measures forward scattering
199 in the angle of 45° . In the instrument manual, it points out that $K = 3.0$ in the
200 Koschmeider equation that connects light extinction and visibility.

201 This automatic measurement is different from the manual measurement before
202 2013, i.e., by human eyes. Manual observations tend to give larger visibility values than
203 automatic measurements, whereas their linear trends are highly consistent (Fan et al.,
204 2017; Liu et al., 2017). Therefore, precaution should be taken when combining manual
205 and automatic visibility measurements for long-term $PM_{2.5}$ studies, which is the focus
206 of our future studies. For example, according to the Koschmeider equation, $AEC=K/V$,

207 $K = -\ln \varepsilon$, and ε denotes visual contrast. According to the regulations of the International
208 Meteorological Organization, $\varepsilon = 0.05$ ($K = 3.0$) for instrument measurement. When
209 manual measurements of visibility are used for historical analyses in future research,
210 we will change the value of K to 3.9 (Lin et al., 2104; Lin and Li, 2016). In addition,
211 we will consider discontinuity issues about long-term visibility data such as site
212 movement and reporting standard. Observations taken at night and under heavy
213 cloudy conditions can also be uncertain. Therefore, a careful filtering and quality
214 control process will be performed before these data are used to study long-term trend.
215 Nevertheless, this study only focuses on the automatic visibility measurements.

216 The visibility observations are hourly data beginning at 00:00 UTC (08:00 Beijing
217 Standard Time). Quality control for visibility data is shown in Sect. 2.4. Other
218 meteorological data are also available hourly. Note that compared to satellite AOD data,
219 visibility data provide a much longer time series of information for $PM_{2.5}$ inference
220 since the 1950s to help evaluate the long-term changes in $PM_{2.5}$ and related health
221 impacts. Compared to $PM_{2.5}$ measurement sites, meteorological stations are spatially
222 more homogeneous and are available at urban, rural and remote areas, providing better
223 spatial representativeness.

224 **2.3 GEOS-Chem model**

225 We used the nested GEOS-Chem model for China (version 11-01,
226 http://wiki.seas.harvard.edu/geos-chem/index.php/Main_Page) to simulate the ratio
227 between surface $PM_{2.5}$ concentration and Aerosol Extinction Coefficient (AEC) for
228 converting the visibility-derived near-surface AEC to $PM_{2.5}$. Driven by the GEOS-FP
229 assimilation meteorology from the Goddard Earth Observing System (GEOS) of the
230 NASA Global Modeling and Assimilation Office, the nested model has a horizontal
231 resolution of 0.3125° longitude x 0.25° latitude with 47 vertical layers, and the lowest
232 10 layers are of ~ 130 m thickness each. The lateral boundary conditions of nested
233 model are taken every 3 hours from a global GEOS-Chem simulation at 2.5°

234 longitude x 2° latitude. Spin-up time for nested model and global model are 15 days
235 and one month, respectively. The scheme of planetary boundary layer employs a
236 non-local scheme implemented by Lin and McElroy (2010). Model convection is
237 simulated with the relaxed Arakawa–Schubert scheme (Rienecker et al., 2008).

238 Both the global and nested GEOS-Chem models are run with the
239 NO_x-O_x-hydrocarbon-aerosol-bromine tropospheric chemistry mechanism with
240 online aerosols. Aerosols simulated include secondary inorganic aerosols (SIOA,
241 including sulfate, nitrate and ammonium), secondary organic aerosols (SOA), primary
242 organic aerosols (POA), black carbon (BC), dust and sea salt. The
243 ammonium-sulfate-nitrate-water system is calculated by ISORROPIA II
244 thermodynamic equilibrium model (Fountoukis and Nenes 2007), with updates on
245 heterogeneous sulfate and nitrate processes (Zhang et al., 2015). Natural dust particles
246 are emitted with the DEAD scheme (Fairlie et al., 2010; Zhang et al., 2013). The
247 calculation of SOA species are parameterized by Pye and Seinfeld (2010). The
248 parameterization of sea salt is from Jaegle et al. (2011). Uptake of the hydroperoxyl
249 radical on aerosols and representation of anthropogenic aromatics follow Lin et al.
250 (2012) and Ni et al. (2018).

251 Monthly gridded anthropogenic emissions in China are taken from the
252 Multi-resolution Emission Inventory for China (MEIC, www.meicmodel.org; Geng et
253 al., 2017) for 2014 for nitrogen oxides (NO_x), carbon monoxide (CO), sulfur dioxide
254 (SO₂), BC and POA. Following Zhang et al. (2015), emissions of anthropogenic fine
255 dust are also included, by taking primary PM_{2.5} emissions from MEIC. For
256 non-methane volatile organic compounds (NMVOC) emissions, the spatial pattern,
257 seasonal pattern and ratios of individual compounds to the total NMVOC are fixed,
258 with the total amount of NMVOC scaled to each specific study year according to the
259 national total amount of NMVOC in MEIC in 2014. Biomass burning emissions are
260 taken from the monthly GFED4 datasets (Giglio et al., 2013). Biogenic emissions of

261 NMVOC follow MEGANv2.1 (Guenther et al., 2012). Soil emissions of NO_x employ
262 the parameterization from Hudman et al. (2012).

263 Future research aiming to combine model simulations with visibility data for
264 historical PM_{2.5} studies could use the MERRA2 assimilated meteorological data
265 available since 1980 and the monthly emission data from the Community Emissions
266 Data System available since 1750. A historical analysis, however, is out of the scope
267 of this study.

268 **2.4 Retrieval method**

269 As shown in Figure 2, our retrieval method contains multiple steps. First, we
270 conducted quality control for visibility data, following previous studies (Husar et al.,
271 2000; Lin et al., 2014; Li et al., 2016). Fine particle matter and relative humidity is the
272 two main factors affecting visibility. Observational results (Chen et al., 2012) show
273 that when $RH < 90\%$, low visibility is largely influenced by aerosol volume
274 concentration; while for $RH > 90\%$, indicative of the formation of fogs and
275 precipitation, the increase of RH is dominantly responsible for the decrease of visibility.
276 Therefore, to reduce the effect of non-aerosol factors on visibility, we excluded
277 visibility records when RH exceeded 90%. This choice is consistent with previous
278 studies (Craig and Faulkenberry, 1979; Zhao et al., 2011). We further excluded data that
279 may be affected by blown snow from the ground, i.e., when air temperature is below
280 $-29\text{ }^{\circ}\text{C}$ and wind speed above 16 km/h. If the maximum value of visibility data at a site
281 in the clean area (median visibility > 11 km) within a month is smaller than 12 km, all
282 data at that site in that month were excluded; this situation indicates erroneous data
283 record. To remove potentially erroneous data spikes, if the daily mean visibility on a
284 day is lower than one third of the value both on the day before and on the day after, data
285 on that day were excluded (Husar et al., 2000).

286 Second, we converted the quality controlled visibility data to hourly near-surface
287 AEC. According to the Koschmieder Equation, near-surface AEC at 550 nm is

288 inversely proportional to visibility if the effect of air molecules is neglected: $AEC =$
 289 K/V . This formula is often used for the conversion between visibility and aerosol
 290 extinction coefficient (Husar et al., 2000; Lin et al., 2014; Xu et al., 2005). Here V
 291 represents the observed visibility, and $K=-\ln\epsilon$ is the Koschmieder constant. For FSVM,
 292 the contrast threshold ϵ is chosen as 5%, with K equal to 3.0 (Li and Sun, 2009; Zeng
 293 and Wang, 1999). In order to reduce the optical influence of air molecules and correct
 294 for other potential errors at clean (high visibility) situations, we used a modified
 295 formula to relate visibility and AEC: $AEC = K/V - K/V_0$, where $V_0 = 70$ km (Lin et al.,
 296 2014).

297 Third, we adopted the hourly ratio of $PM_{2.5}$ to AEC simulated by GEOS-Chem to
 298 scale the visibility converted AEC to obtain the visibility-inferred $PM_{2.5}$ concentrations
 299 at individual sites (hereafter referred to as Station Concerted- $PM_{2.5}$):

$$300 \quad (PM_{2.5})_{SC} = AEC \cdot \frac{(PM_{2.5})_{model}}{AEC_{model}}$$

301 For a particular site, the modeled ratio of $PM_{2.5}$ to AEC was taken as the value
 302 interpolated from nearby model grid cells through bilinear interpolation, with the time
 303 of model results matching that of the hourly visibility data. At each model grid cell, the
 304 model $PM_{2.5}$ concentration was summed over the concentrations of fine dust (DST1 +
 305 $0.38 \times$ DST2 in the model), fine sea salt particles (SALA in the model), BC, POA
 306 (assumed to be 1.8 times the mass of primary organic carbon), and SIOA. The model
 307 AEC was calculated based on the optical effects of these $PM_{2.5}$ components and
 308 additional coarse mode dusts (DST3 and DST4) and coarse sea salt particles (SALC),
 309 with their hygroscopicity accounted for (Lin et al., 2016) using the observed RH at
 310 respective meteorological station. Inclusion of coarse particles in calculating model
 311 AEC ensures the consistency with visibility-inferred AEC that is affected by both fine
 312 and coarse particles. Considering that the measured $PM_{2.5}$ and visibility data are
 313 near-surface, we choose the values of model $PM_{2.5}$ and AEC in the bottom model layer

314 (i.e., from the ground to approximately 130 m). Then, we obtained a Station-Converted
315 hourly $PM_{2.5}$ dataset in January, April, July and October 2014 over the NCP. The daily
316 mean $PM_{2.5}$ data were averaged from the hourly data.

317 Fourth, we converted the station-specific daily mean $PM_{2.5}$ data to gridded data at
318 a horizontal resolution of 0.3125° longitude \times 0.25° latitude, according to the resolution
319 of GEOS-Chem. The resulting dataset is referred to as Grid-Converted $PM_{2.5}$. There are
320 two purposes for this station-to-grid conversion. The station-based data lack continuous
321 spatial coverage needed for health impacts studies. Also, the station-based visibility
322 measurements are subject to instrument errors and representation errors, i.e., the
323 measured values may be affected by local pollution sources and other factors and thus
324 not fully representative of the actual pollution level in the surrounding area. In fact,
325 visibility data may contain certain “noise” spatially, as shown in Lin et al. (2014) and in
326 Sect. 3.3.

327 We tested 8 candidate methods for this station-to-grid conversion, and finally
328 selected a method, Case 7, that has the best performance; see below for evaluation
329 statistics and Sect. 3.2 for the selection process. All cases but Case 2 and Case 3
330 involved matching a grid cell center to surrounding visibility stations within a certain
331 radius. We tested radii of 0.1° , 0.2° , 0.3° , 0.4° , 0.5° , 0.6° , 0.7° , 0.8° , 0.9° , 1.0° , 1.5°
332 and 2° . The larger the radius is, the higher extent the Station-Converted $PM_{2.5}$ data are
333 spatially smoothed.

$$\text{Case1: } c_{d,i}^F = \text{median}(c_{d,i}^{SC})$$

$$\text{Case2: } c_{d,i}^F = c_{d,i}^{Cres}$$

$$\text{Case3: } c_{d,i}^F = \frac{\prod_{i=1}^n r_i^{-1}}{\sum_{i=1}^n r_i^{-1}} c_{d,i}^{SC}$$

$$\text{Case4: } c_{d,i}^F = \text{median}\left(\frac{c_{d,i}^{SC}}{c_{d,i}^M}\right) c_{d,i}^M$$

$$\text{Case5: } c_{d,i}^F = \frac{\text{median}(c_{m,i}^{SC})}{c_{m,i}^M} c_{d,i}^M$$

$$\text{Case6: } c_{d,i}^F = \frac{c_{m,i}^M}{\text{median}(c_{m,i}^{SC})} \text{median}(c_{d,i}^{SC})$$

$$\text{Case7: } c_{d,i}^F = \frac{c_{m,i}^M / \text{mean}(c_{m,i}^M)}{c_{m,i}^{SC} / \text{mean}(c_{m,i}^{SC})} \text{median}(c_{d,i}^{SC})$$

$$334 \quad \text{Case8: } c_{d,i}^F = \frac{c_{m,i}^M / \text{mean}(c_{m,i}^M)}{c_{m,i}^{Cres} / \text{mean}(c_{m,i}^{Cres})} c_{d,i}^{Cres}$$

335 In these eight candidate methods to convert station-specific to gridded PM_{2.5}
 336 data, $c_{d,i}^F$ denotes the finally obtained daily mean PM_{2.5} concentration on day d at
 337 grid cell i. The superscript F denotes final, M denotes model, SC denotes Station
 338 Converted, and Cres denotes Cressman interpolation. The subscript r denotes distance,
 339 d denotes day, m denotes month, i denotes grid cell i, and i' denotes the grid cell in
 340 which the visibility measurement station is located. The function “mean” denotes the
 341 average over all grid cells, and “median” denotes the median value among the
 342 selected grid cells.

343 Of these 8 methods, Cases 1-3 utilized the Station-Converted PM_{2.5} data alone
 344 without further using GEOS-Chem simulations. Case 1 assigned to a grid cell the
 345 median value from stations within a certain radius of the grid cell center. Cases 2 and 3
 346 used the Cressman and the Inverse Distance Weight (IDW) interpolation methods,
 347 respectively.

348 Cases 4-8 used the spatial variability simulated by GEOS-Chem to facilitate the
 349 station-to-grid conversion. As shown in Sect. 3.1, the GEOS-Chem simulated spatial

350 distribution of $PM_{2.5}$ outperforms the distribution of visibility-converted station-based
351 data. In Case 4, for a given grid cell “i” on each day, we found all stations within a
352 certain radius of the grid cell center, calculated the ratios of Station-Converted $PM_{2.5}$ to
353 Modeled $PM_{2.5}$ (at the grid cells in which these visibility stations are located), and
354 then used the median value of these ratios to scale the Modeled $PM_{2.5}$ at grid cell “i”.
355 Case 5, aiming to eliminate the noise in the day-to-day variability, was similar to Case 4
356 except that the ratios were based on monthly (rather than daily) mean $PM_{2.5}$ data. Here,
357 to reduce the monthly average calculation errors caused by missing values, we chose
358 the median value of all stations within a certain radius of the grid cell center to match
359 the model $PM_{2.5}$, and then used data on the days when Station-Converted $PM_{2.5}$ and
360 model $PM_{2.5}$ are both available. Case 6 was similar to Case 5, except that the scaling
361 was based on the (spatial) median of Station-Converted $PM_{2.5}$ data.

362 Cases 7 and Case 8 were designed based on the fact that Modeled $PM_{2.5}$ data were
363 spatially consistent with $PM_{2.5}$ measurements and had a lower mean bias (see Sect. 3.1).
364 The two cases used the spatial pattern (shape) of model $PM_{2.5}$ data to facilitate the
365 station-to-grid conversion. For Case 7, we first calculated the monthly Modeled $PM_{2.5}$
366 at each grid cell normalized to its spatial average, calculated the respective value for
367 Station-Converted $PM_{2.5}$, and then derived their ratio. The calculation of monthly
368 mean values and the sampling of available grid cells were the same as in Case 5. We
369 then used this ratio to scale the result derived from Case 1 to finally obtain the gridded
370 and spatial shape-adjusted daily $PM_{2.5}$ data. Case 8 was similar to Case 7, except that
371 Station-Converted $PM_{2.5}$ data are replaced by Cressman-interpolated gridded data from
372 Case 2.

373 Evaluation of the 8 station-to-grid conversion methods was based on how each
374 method led to high spatial and temporal (i.e., day-to-day across the four months)
375 consistencies with the actual $PM_{2.5}$ measurements. A few indicators were used to
376 evaluate the consistency, including bias, correlation coefficient, slope of a linear

377 regression, root mean square error (RMSE). We applied the Reduced Major Axis
378 (RMA) regression, which is more appropriate than the Ordinary Least Square
379 regression when independent variable x contains errors, to estimate the slope and
380 intercept.

381 **3. Spatio-temporal variability of Measured, Modeled, Station-Converted and** 382 **Grid-Converted PM_{2.5}**

383 **3.1 Comparison of Station-Converted, Modeled and Measured PM_{2.5}**

384 Figure 3 compares the spatial distributions of (a) observed, (b) Station-Converted,
385 (c) Station-Converted and sampled based on available observations, (d) modeled and
386 (e) Grid-Converted PM_{2.5} concentrations over the NCP averaged over January, April,
387 July and October 2014. From the observed data (Fig. 3a), which represent urban air
388 quality, high PM_{2.5} pollution occur over southern Hebei. The highest PM_{2.5}
389 concentrations reach 170.4 $\mu\text{g}/\text{m}^3$, due to the combined effects of large emissions,
390 efficient secondary formation and unfavorable conditions for pollution outflow. PM_{2.5}
391 concentrations are lower over the northern parts of Hebei and Shanxi, Shandong
392 Peninsula and Inner Mongolia, due to lower emissions and favorable topographical and
393 meteorological conditions for pollution removal/transport (Zheng et al., 2018; Zhang et
394 al., 2018). The domain average PM_{2.5} concentration is 83.8 $\mu\text{g}/\text{m}^3$.

395 Figure 3b shows the Station-Converted PM_{2.5} data, which are more much
396 regionally representative than the PM_{2.5} observations (Fig. 3a) and still capture the
397 observed spatial pattern (from urban sites). Since the Station-Converted PM_{2.5} data are
398 not spatially collocated with PM_{2.5} observations, we choose the median value of the
399 converted PM_{2.5} data from all stations within a 0.2° radius of each PM_{2.5} observation
400 station (Fig. 3c). Such re-sampled data reveal several locations where
401 Station-Converted PM_{2.5} overestimate the observed values significantly. Averaged over
402 the NCP, the Station-Converted concentration is 109.8 $\mu\text{g}/\text{m}^3$, with an overestimate by
403 26.0 $\mu\text{g}/\text{m}^3$. The scatter plots in Fig. 4 also show significant positive biases of

404 Station-Converted $PM_{2.5}$ data, especially when the pollutant concentrations are high.

405 GEOS-Chem captures the observed spatial distribution of $PM_{2.5}$ concentrations
406 averaged over the four months in 2014 (Fig. 3d). As for model and Grid-Converted
407 $PM_{2.5}$, we match the observation by choosing the grid cell in which the observation
408 station is located. In particular, Figure 4a shows that when sampled coincidentally with
409 the observations, the modeled $PM_{2.5}$ results have a small positive bias (by $2.5 \mu\text{g}/\text{m}^3$).
410 The model has a high spatial correlation coefficient (0.73) with the observed data, much
411 higher than the correlation coefficient for the Station-Converted data (0.49) (Fig. 4b).
412 The modeled data also have significantly lower RMSE than the Station-Converted data
413 (Fig. 4a and 4b). These results suggest that the model better captures the spatial
414 distribution of $PM_{2.5}$ observations than the visibility-based data do.

415 Figure 5 further evaluates the day-to-day variations of modeled and
416 Station-Converted $PM_{2.5}$ concentrations against the observations in the four months.
417 Modeled and Station-Converted data were sampled based on the observations; and
418 results were averaged over the NCP on each day. Although both the modeled and
419 Station-Converted $PM_{2.5}$ can capture the day-to-day variation of the observed data, the
420 capability of Station-Converted data is better, especially with a higher correlation
421 coefficient (0.96 versus 0.84). However, the modeled data is better than the
422 Station-Converted ones in terms of mean bias and RMSE. Note that because of the
423 difference in data averaging, the values for bias here are slightly different from those
424 in the discussion of spatial distribution.

425 **3.2 Evaluation of Grid-Converted $PM_{2.5}$ data derived from 8 candidate** 426 **station-to-grid mapping methods**

427 This section evaluates the Grid-Converted $PM_{2.5}$ data derived from 8 candidate
428 station-to-grid mapping approaches presented in Sect. 2.4. Such mapping is based on
429 the preference for health impact studies to having high spatial coverage and, for a few
430 mapping approaches, an attempt to take advantage of the GEOS-Chem model

431 capability in capturing the spatial pattern of $PM_{2.5}$ observations. As mentioned in Sect.
432 2.4, the evaluation focuses on whether the Grid-Converted data can capture both the
433 spatial and temporal (day-to-day) variations of observed $PM_{2.5}$.

434 Figure 6 shows the evaluation statistics for each case, as a function of the distance
435 (radius) from the visibility station to the grid cell center. As the mapping radius
436 increases, the spatial feature of Grid-Converted $PM_{2.5}$ is further smoothed and the
437 spatial details are further lost. For temporal (day-to-day) correlation evaluation (Fig.
438 6b), data on each day are averaged over all $PM_{2.5}$ measurement sites. In general,
439 results for temporal correlation do not show a strong dependence on the mapping
440 radius, mainly because $PM_{2.5}$ data are spatially averaged. For all cases and radii, the
441 temporal correlation coefficients exceed 0.8, reflecting that the Station-Converted
442 $PM_{2.5}$ data have a good performance in terms of temporal variation. However, Cases 2,
443 3, 7 and 8 still outperform the other cases ($R > 0.9$ for all radii). Evaluation on
444 temporal bias gives a similar result to the evaluation on spatial bias (see below) and is
445 thus not shown.

446 For evaluation of spatial bias and correlation (Fig. 6a, and c), data at each $PM_{2.5}$
447 measurement site were averaged over the four months. The biases of Cases 1, 4 and 5
448 are very sensitive to the mapping radius, and the lowest biases are obtained for a
449 radius of 0.5° – 0.6° . These three cases also result in relatively low spatial correlation
450 coefficients (< 0.6). Cases 1 and 5 have similar results. Case 2 (with Cressman
451 interpolation) leads to a relative high bias, except when the mapping radius exceeds
452 0.7° . Case 3 is derived from the IDW method, and thus its evaluation results do not
453 vary with the mapping radius. Case 3 has a relatively low spatial correlation ($R = 0.60$)
454 and a high bias ($13.6 \mu\text{g}/\text{m}^3$). Case 6 leads to the smallest mean bias, and its respective
455 correlation coefficient is among the highest and does not change significantly with
456 radius. Case 7 has the second highest spatial correlation coefficient (after Case 8) and
457 a relatively small bias (within $10 \mu\text{g}/\text{m}^3$ when radius is greater than 0.2°). This low

458 bias suggests that using GEOS-Chem simulation results to adjust the spatial
459 distribution of visibility inferred $PM_{2.5}$ helps to reduce the bias, a desirable outcome.
460 Case 8 leads to the highest correlation coefficient, but it also has the greatest bias (> 30
461 $\mu\text{g}/\text{m}^3$ for all mapping radius).

462 Figure 6d further shows the RMA regression slope for the spatial variability of
463 temporally averaged Grid-Converted $PM_{2.5}$ data. The slope of Case 8 is the highest
464 and has small dependence on radius (i.e., between 1.35 and 1.40). The slopes of Case
465 1, 4 and 5 decline significantly with the increasing radius. Although Case 6 has the
466 smallest mean bias and a high correlation coefficient, the regression slope of Case 6 is
467 relatively low (< 0.75) for all radii. The slope of Case 7 declines slightly with the
468 increasing radius, and it remains between 0.85 and 1.05 for all radii.

469 Overall, Case 7 with a mapping radius of 0.3° has the most desired performance
470 in both the temporal and the spatial domains. In particular, it has a relatively small mean
471 bias ($7.9 \mu\text{g}/\text{m}^3$, or 9.4%), high correlation coefficients (0.80 spatially and 0.96
472 temporally) and better slope (1.0 spatially). A radius of 0.3° also helps preserve the
473 high-resolution spatial information embedded in the visibility data and GEOS-Chem
474 simulations. In the next section, we analyze the gridded results from this method in
475 detail.

476 **3.3 Spatio-temporal distribution of Grid-Converted $PM_{2.5}$ based on the** 477 **selected station-to-grid conversion method (Case 7)**

478 Figure 3e shows the gridded distribution of $PM_{2.5}$ concentrations averaged over
479 the four months in 2014 based on Case 7 with a mapping radius of 0.3° . The spatial
480 distribution is consistent with the observed one, such as the highest $PM_{2.5}$
481 concentrations over southern Hebei and the lowest over the northern regions. The
482 gridded dataset corrects the underestimate in the model results and reduces the
483 excessively high values in the Station-Converted data.

484 The scatter plots in Figure 4c further evaluate the spatial distribution of
485 Grid-Converted (Case 7) data against $PM_{2.5}$ observations. Gridded data were sampled
486 from the grid cells covering the $PM_{2.5}$ measurement stations and on days with available
487 $PM_{2.5}$ measurements. The correlation coefficient ($R = 0.80$) with the observed $PM_{2.5}$
488 are higher than model simulations ($R = 0.73$) and Station-Converted $PM_{2.5}$ ($R = 0.49$)
489 alone. The mean bias ($7.9 \mu\text{g}/\text{m}^3$, or 9.4%), the RMA regression slope (1.0), and the
490 small RMSE ($17.6 \mu\text{g}/\text{m}^3$) are also desirable, compared to the values for GEOS-Chem
491 simulations ($2.5 \mu\text{g}/\text{m}^3$, 0.80, and $18.6 \mu\text{g}/\text{m}^3$, respectively) and Station-Converted
492 data ($25.7 \mu\text{g}/\text{m}^3$, 1.8, and $51.1 \mu\text{g}/\text{m}^3$, respectively).

493 Figure 5c shows the day-to-day variations of observed and Grid-Converted $PM_{2.5}$
494 concentrations (Case 7) in each month. For each day, data were selected from stations
495 with available observations and converted values, and were further averaged over the
496 NCP. Figure 5c shows that Grid-Converted $PM_{2.5}$ data have a small bias of $9.4 \mu\text{g}/\text{m}^3$
497 (or 11.4%); note that this value is slight different from the spatial bias ($7.9 \mu\text{g}/\text{m}^3$, or
498 9.4%) because of the difference between temporal and spatial sampling. The temporal
499 variation of Grid-Converted $PM_{2.5}$ over the four months is consistent with the observed
500 variation ($R = 0.96$, linear regression slope = 1.0), better than that of GEOS-Chem (R
501 = 0.84, slope = 0.70) and Station-Converted ($R = 0.96$, slope = 1.3) $PM_{2.5}$. The
502 Grid-Converted $PM_{2.5}$ data also capture the observed $PM_{2.5}$ peaks, which represent the
503 pollution episodes, as well as the low values on clean days. They reproduce the
504 seasonal variation of observed $PM_{2.5}$ mass concentrations, i.e., a higher mean value
505 and day-to-day variability in winter and lower values in summer. The Grid-Converted
506 $PM_{2.5}$ correct the temporally consistent overestimate in the Station-Converted $PM_{2.5}$
507 data and the wintertime underestimate and summertime overestimate in GEOS-Chem
508 simulations.

509 4. Conclusions

510 This study offers a novel, plausible method to infer surface $PM_{2.5}$ mass

511 concentrations on a 0.3125° longitude x 0.25° latitude grid, by combining the spatially
512 dense high-frequency surface visibility measurements and GEOS-Chem simulations.
513 Applying the method to the NCP in January, April, July and October 2014 shows good
514 performance of the inferred data with respect to the official $PM_{2.5}$ measurements.

515 Specifically, after the visibility data are converted to $PM_{2.5}$ concentrations at each
516 station and then each grid cell (based on Case 7 with a mapping radius of 0.3°), the
517 derived gridded $PM_{2.5}$ data are both spatially and temporally consistent with the $PM_{2.5}$
518 measurements. The spatial and temporal mean biases are both within $10 \mu\text{g}/\text{m}^3$. The
519 temporal (day-to-day) correlation coefficient reaches 0.96 with a linear regression
520 slope of 1.0. The spatial correlation coefficient reaches 0.80 with a regression slope of
521 1.0. The lower spatial correlation than the temporal correlation reflects that visibility
522 data are spatially noisier (Lin and Li, 2016). Grid-Converted $PM_{2.5}$ improves upon
523 GEOS-Chem simulations by correcting its wintertime underestimate and summertime
524 overestimate. The temporal correlation coefficient, temporal regression slope, spatial
525 correlation coefficient and spatial regression slope of converted $PM_{2.5}$ data are better
526 than GEOS-Chem simulation results (0.84, 0.70, 0.73 and 0.80, respectively).

527 Future research will apply the inference method to all months in multiple years in
528 the NCP to further test the robustness of the conversion method proposed here, with
529 the goal of finally applying the method for a reliable retrieval of multi-decadal $PM_{2.5}$
530 variability embedded in the visibility data.

531 **Acknowledgments**

532 This work was supported by the National Natural Science Foundation of China
533 [grant numbers 41831175, 41775115, 41425019, and 41721004]. We acknowledge
534 China Meteorology Administration (CMA) and China National Environmental
535 Monitoring Centre (CNEMC) for visibility and $PM_{2.5}$ data, respectively.

536 **References**

- 537 Allen, R.J., Norris, J.R., Kovilakam, M., 2014. Influence of anthropogenic aerosols
538 and the Pacific Decadal Oscillation on tropical belt width. *Nat. Geosci.* 7, 270–274.
- 539 Boys, B.L., Martin, R.V., van Donkelaar, A., MacDonell, R.J., Hsu, N.C., Cooper,
540 M.J., Yantosca, R.M., Lu, Z., Streets, D.G., Zhang, Q., Wang, S.W., 2014.
541 Fifteen-year global time series of satellite-derived fine particulate matter. *Environ Sci*
542 *Technol.* 48, 11109-11118.
- 543 Charlson, R.J., 1969. Visibility Related to Aerosol Mass Concentration - A Review.
544 *Environment Science & Technology* 3, 913-918.
- 545 Chen, J., Zhao, C., Ma, N., Liu, P., Gobel, T., Hallbauer, E., Deng, Z., Ran, L., Xu, W.,
546 Liang, Z., 2012. A parameterization of low visibilities for hazy days in the North
547 China Plain. *Atmospheric Chemistry and Physics* 12, 4935-4950.
- 548 Chen, Y.-z., Zhao, D., Chai, F.-h., Liang, G.-x., Xue, Z.-g., Wang, B.-b., Liang, Y.-j.,
549 Chen, Y., Zhang, M., 2010. Correlation between the atmospheric visibility and aerosol
550 fine particle concentrations in Guangzhou and Beijing. *China Environmental Science*
551 30, 967-971.
- 552 Craig, C.D., Faulkenberry, G.D., 1979. Application of ridit analysis to detect trends in
553 visibility. *Atmospheric Environment* 13, 1617-1622.
- 554 Fairlie, T.D., D.J. Jacob, J.E. Dibb, B. Alexander, M.A. Avery, A. van Donkelaar, and
555 L. Zhang, 2010. Impact of mineral dust on nitrate, sulfate, and ozone in transpacific
556 Asian pollution plumes. *Atmos. Chem. Phys.* 10, 3999-4012.
- 557 Fan, G., Ren, L., Mao, Y., 2017. Reconstruction of haze day database based on the
558 comparison between manual and automatic observations. *China Environmental*
559 *Science* 37, 1254-1261.
- 560 Fountoukis, C., Nenes, A., 2007. ISORROPIA II: a computationally efficient

- 561 thermodynamic equilibrium model for K^+ - Ca^{2+} - Mg^{2+} - NH_4^+ - Na^+ - SO_4^{2-} - NO_3^- - Cl^- -
562 H_2O aerosols. *Atmos. Chem. Phys.* 7, 4639–4659.
- 563 Ge, B., Wang, Z., Lin, W., Xu, X., Li, J., Ji, D., Ma, Z., 2018. Air pollution over the
564 North China Plain and its implication of regional transport: A new sight from the
565 observed evidences. *Environ Pollut.* 234, 29-38.
- 566 Geng, G., Zhang, Q., Martin, R.V., van Donkelaar, A., Huo, H., Che, H., Lin, J., He,
567 K., 2015. Estimating long-term $PM_{2.5}$ concentrations in China using satellite-based
568 aerosol optical depth and a chemical transport model. *Remote Sensing of*
569 *Environment.* 166, 262-270.
- 570 Geng, G., Zhang, Q., Martin, R. V., Lin, J.-T., Huo, H., Zheng, B., Wang, S., and He,
571 K., 2017. Impact of spatial proxies on the representation of bottom-up emission
572 inventories: A satellite-based analysis. *Atmospheric Chemistry and Physics.* 17,
573 4131-4145.
- 574 Giglio, L., J. T. Randerson, and G. R. van der Werf, 2013. Analysis of daily, monthly,
575 and annual burned area using the fourth-generation global fire emissions database
576 (GFED4)", *J. Geophys. Res, Biogeosciences.* 118, Issue 1, 317-328.
- 577 Guenther, A. B., Jiang, X., Heald, C. L., Sakulyanontvittaya, T., Duhl, T., Emmons, L.
578 K., and Wang, X., 2012. The Model of Emissions of Gases and Aerosols from Nature
579 version 2.1 (MEGAN2.1): an extended and updated framework for modeling biogenic
580 emissions. *Geosci. Model Dev.* 5, 1471-1492.
- 581 Hudman, R.C., N.E. Moore, R.V. Martin, A.R. Russell, A.K. Mebust, L.C. Valin, and
582 R.C. Cohen, 2012. A mechanistic model of global soil nitric oxide emissions:
583 implementation and space based-constraints. *Atm. Chem. Phys.* 12, 7779-7795.
- 584 Husar, R.B., Husar, J.D., Martin, L., 2000. Distribution of continental surface aerosol
585 extinction based on visual range data. *Atmospheric Environment.* 34, 5067-5078.

- 586 Jaegle, L., Quinn, P. K., Bates, T. S., Alexander, B., and Lin, J.-T., 2011. Global
587 distribution of sea salt aerosols: new constraints from in situ and remote sensing
588 observations. *Atmos. Chem. Phys.* 11, 3137-3157.
- 589 Lelieveld, J., Evans, J.S., Fnais, M., Giannadaki, D., Pozzer, A., 2015. The contribution
590 of outdoor air pollution sources to premature mortality on a global scale. *Nature.* 525,
591 367–371.
- 592 Li Hao, Sun, X., 2009. Theoretical analysis on measurement error of forward
593 scattering visibility meter. *Infrared and Laser Engineering.* 38, 1094-1098.
- 594 Li, J., C.Li, C. Zhao, T.Su, 2016. Changes in surface aerosol extinction trends over
595 China during 1980-2013 inferred from quality-controlled visibility data. *Geophysical*
596 *Research Letters.* 43, 8713-8719.
- 597 Li, T., Shen, H., Yuan, Q., Zhang, X., Zhang, L., 2017. Estimating groundlevel PM_{2.5}
598 by fusing satellite and station observations: A geo-intelligent deep learning approach.
599 *Geophysical Research Letters.* 44, 11985-11993.
- 600 Liao, H., Henze, D.K., Seinfeld, J.H., Wu, S., Mickley, L.J., 2007. Biogenic
601 secondary organic aerosol over the United States: comparison of climatological
602 simulations with observations. *J. Geophys. Res. Atmos.* 112, D06201.
- 603 Lim, S.S., Vos, T., Flaxman, A.D., 2012. A comparative risk assessment of burden of
604 disease and injury attributable to 67 risk factors and risk factor clusters in 21 regions,
605 1990-2010: a systematic analysis for the global burden of disease study 2010. *Lancet,*
606 381, 1276-1276.
- 607 Lin, J.-T., Liu, Z., Zhang, Q., Liu, H., Mao, J., and Zhuang, G., 2012. Modeling
608 uncertainties for tropospheric nitrogen dioxide columns affecting satellite-based
609 inverse modeling of nitrogen oxides emissions. *Atmospheric Chemistry and Physics.*
610 12, 12255-12275.

- 611 Lin, J., McElroy, M.B., 2010. Impacts of boundary layer mixing on pollutant vertical
612 profiles in the lower troposphere: Implications to satellite remote sensing.
613 *Atmospheric Environment*. 44, 1726-1739.
- 614 Lin, J.-T., McElroy, M. B., and Boersma, K. F., 2010. Constraint of anthropogenic
615 NO_x emissions in China from different sectors: a new methodology using multiple
616 satellite retrievals. *Atmos. Chem. Phys.* 10, 63–78.
- 617 Lin, J., Li, J., 2016. Spatio-temporal variability of aerosols over East China inferred
618 by merged visibility-GEOS-Chem aerosol optical depth. *Atmospheric Environment*.
619 132, 111-122.
- 620 Lin, J., Tong, D., Davis, S., Ni, R., Tan, X., Pan, D., Zhao, H., Lu, Z., Streets, D.,
621 Feng, T., Zhang, Q., Yan, Y., Hu, Y., Li, J., Liu, Z., Jiang, X., Geng, G., He, K., Huang,
622 Y., Guan, D., 2016. Global climate forcing of aerosols embodied in international trade.
623 *Nature Geoscience*. 9, 790-794.
- 624 Lin, J., van Donkelaar, A., Xin, J., Che, H., Wang, Y., 2014. Clear-sky aerosol optical
625 depth over East China estimated from visibility measurements and chemical transport
626 modeling. *Atmos Environ*. 95, 258–267.
- 627 Liu, M., Bi, J., Ma, Z., 2017. Visibility-Based PM_{2.5} Concentrations in China:
628 1957-1964 and 1973-2014. *Environ Sci Technol*. 51(22), 13161-13169.
- 629 Liu, M., Lin, J., Wang, Y., Sun, Y., Zheng, B., Shao, J., Chen, L., Zheng, Y., Chen, J.,
630 Fu, T.-M., Yan, Y., Zhang, Q., and Wu, Z., 2018. Spatiotemporal variability of
631 NO₂ and PM_{2.5} over Eastern China: observational and model analyses with a novel
632 statistical method. *Atmos. Chem. Phys.* 18, 12933-12952.
- 633 Liu, N., Ma, Y., Wang, Y., Liu, X., 2010. Mass Concentration Variation of
634 Atmospheric Particles and Relationship with Visibility in Dandong. *Research of*
635 *Environmental Sciences* 23, 642-646.

- 636 Liu, X., Liu, H., Hong, Z., Qin, Y., 2017. Comparative Analysis of Visibility Data
637 between Automatic and Manual Observation. *Journal of Guizhou Meteorology* 41(6),
638 72-75.
- 639 Ma, Z., Hu, X., Huang, L., Bi, J., Liu, Y., 2014. Estimating ground-level PM_{2.5} in China
640 using satellite remote sensing. *Environmental Science & Technology*. 48, 7436-7444.
- 641 Ni, R.-J., Lin, J.-T., Yan, Y.-Y., and Lin, W., 2018. Foreign and domestic contributions
642 to springtime ozone over China. *Atmospheric Chemistry and Physics*. 18,
643 11447-11469.
- 644 Pye, H.O.T., Seinfeld, J.H., 2010. A global perspective on aerosol from low-volatility
645 organic compounds. *Atmospheric Chemistry and Physics*. 10, 4377-4401.
- 646 Rienecker, M.M., Suarez, M.J., Todling, R., Bacmeister, J., Takacs, L., Liu, H.-C., Gu,
647 W., Sienkiewicz, M., Koster, R.D., Gelaro, R., Stajner, I., Nielsen, E., 2008. The
648 GEOS-5 Data Assimilation System Documentation of Versions 5.0.1, 9.1.0, and
649 5.2.0. NASA.
- 650 Shen, Z.X., Cao, J.J., Zhang, L.M., Zhang, Q., Huang, R.J., Liu, S.X., Zhao, Z.Z., Zhu,
651 C.S., Lei, Y.L., Xu, H.M., Zheng, C.L., 2016. Retrieving historical ambient PM_{2.5}
652 concentrations using existing visibility measurements in Xi'an, Northwest China.
653 *Atmospheric Environment*. 126, 15-20.
- 654 Sinclair, D., Countess, R.J., Hoopes, G.S., 1974. Effect of relative humidity on the
655 size of atmospheric aerosol particles. *Atmospheric Environment* (1967) 8, 1111-1117.
- 656 Song, Y., Tang, X., Fang, C., Zhang, Y., Hu, M., Zeng, L., Li, C., Michael, B., 2003.
657 Relationship between the visibility degradation and particle pollution in Beijing. *Acta*
658 *Scientiae Circumstantiae*. 23, 468-471.
- 659 Sun, X., Wang, X., Li, H., Zhang, W., Yan, W., 2009. Atmospheric detection [M].
660 China Meteorological Press, 62.

- 661 Tan, H., Chen, H., Wu, D., Deng, X., Deng, T., Li, F., Zhao, X., Bi, X., 2010. The
662 performance evaluation and data correction of the forward scattering visibility sensor.
663 *Journal of tropical meteorology* 26(6), 687-693.
- 664 van Donkelaar, A., Martin, R.V., Brauer, M., Kahn, R., Levy, R., Verduzco, C.,
665 Villeneuve, P.J., 2010. Global estimates of ambient fine particulate matter
666 concentrations from satellite-based aerosol optical depth: development and application.
667 *Environ Health Perspect.* 118, 847-855.
- 668 van Donkelaar, A., Martin, R.V., Spurr, R.J., Burnett, R.T., 2015. High-Resolution
669 Satellite-Derived PM_{2.5} from Optimal Estimation and Geographically Weighted
670 Regression over North America. *Environ Sci Technol.* 49, 10482-10491.
- 671 Wang, J., Liu, X., 2006. The discussion on relationship between visibility and mass
672 concentration of PM_{2.5} in Beijing. *Acta Meteorol. Sin. (China)* 64, 221-228.
- 673 Wang, Y.H., Liu, Z.R., Zhang, J.K., Hu, B., Ji, D.S., Yu, Y.C., Wang, Y.S., 2015.
674 Aerosol physicochemical properties and implications for visibility during an intense
675 haze episode during winter in Beijing. *Atmospheric Chemistry and Physics.* 15,
676 3205-3215.
- 677 Wang, Y.H., Hu, B., Ji, D. S., Liu, Z. R., Tang, G. Q., Xin, J. Y., Zhang, H. X., Song, T.,
678 Wang, L. L., Gao, W. K., Wang, X. K., and Wang, Y. S., 2014. Ozone weekend effects
679 in the Beijing–Tianjin–Hebei metropolitan area, China. *Atmos. Chem. Phys.*
680 14,2419-2429.
- 681 Wei, J., Huang, W., Li, Z., Xue, W., Peng, Y., Sun, L., Cribb, M., 2019. Estimating
682 1-km-resolution PM_{2.5} concentrations across China using the space-time random
683 forest approach. *Remote Sensing of Environment* 231, 111221.
- 684 Wu, H., Tang, X., Wang, Z., Wu, L., Lu, M., Wei, L., Zhu, J., 2018. Probabilistic
685 Automatic Outlier Detection for Surface Air Quality Measurements from the China
686 National Environmental Monitoring Network. *Advances in Atmospheric Sciences.* 35,

- 687 1522-1532.
- 688 Xu, P., Tan, X., Cai, J., Liu, J., 2005. Study on influence factors of urban aerosol on
689 visibility & extinction coefficient. *Environmental Pollution & Control* 27(6), 410-413.
- 690 Zeng, S., Wang, G., 1999. Observation and instrument of visibility. *Quarterly Journal*
691 *of Applied Meteorology* 10(2), 6, 207-212.
- 692 Zhao, P.S., Zhang, X.L., Xu, X.F., Zhao, X.J., 2011. Long-term visibility trends and
693 characteristics in the region of Beijing, Tianjin, and Hebei, China. *Atmos. Res.* 101,
694 711-718.
- 695 Zhang L., Liu, L., Zhao, Y.H., Gong, S.L., Zhang, X.Y., D. K. Henze, S. L. Capps,
696 Tzung-May Fu, Zhang, Q., Wang, Y.X., 2015. Source attribution of particulate matter
697 pollution over North China with the adjoint method. *Environ Res Lett.* 10, 084011.
- 698 Zhang, L., J. F. Kok, D. K. Henze, Q. Li, and C. Zhao, 2013. Improving simulations
699 of fine dust surface concentrations over the western United States by optimizing the
700 particle size distribution. *Geophys. Res. Lett.* 40, 3270–3275.
- 701 Zhang L., Liu W., Lin J., Hou K., Zhang L., Huang B., Rhine W., Wang J., Wang Y.,
702 Jiao Y., Wang Z., Ni R. Liu M., Wang Y., 2019. Air pollution exposure and neonatal
703 jaundice. *Nature Communications*, accepted.
- 704 Zhang, Q., Jiang, X., Tong, D., Davis, S.J., Zhao, H., Geng, G., Feng, T., Zheng, B., Lu,
705 Z., Streets, D.G., Ni, R., Brauer, M., van Donkelaar, A., Martin, R. V, Huo, H., Liu, Z.,
706 Pan, D., Kan, H., Yan, Y., Lin, J., He, K., Guan, D., 2017. Transboundary health
707 impacts of transported global air pollution and international trade. *Nature.*
708 543(7647),705–709.
- 709 Zhang, Z., Xu, X., Qiao, L., Gong, D., Kim, S.J., Wang, Y., Mao, R., 2018. Numerical
710 simulations of the effects of regional topography on haze pollution in Beijing article.
711 *Sci. Rep.* 8:5504.

- 712 Zheng, B., Tong, D., Li, M., Liu, F., Hong, C., Geng, G., Li, H., Li, X., Peng, L., Qi,
713 J., Yan, L., Zhang, Y., Zhao, H., Zheng, Y., He, K., Zhang, Q., 2018. Trends in China's
714 anthropogenic emissions since 2010 as the consequence of clean air actions. *Atmos.*
715 *Chem. Phys. Discuss.* 1–27.
- 716 Zheng, Y., Zhang, Q., Liu, Y., Geng, G., He, K., 2016. Estimating ground-level $PM_{2.5}$
717 concentrations over three megalopolises in China using satellite-derived aerosol
718 optical depth measurements. *Atmospheric Environment.* 124, 232-242.

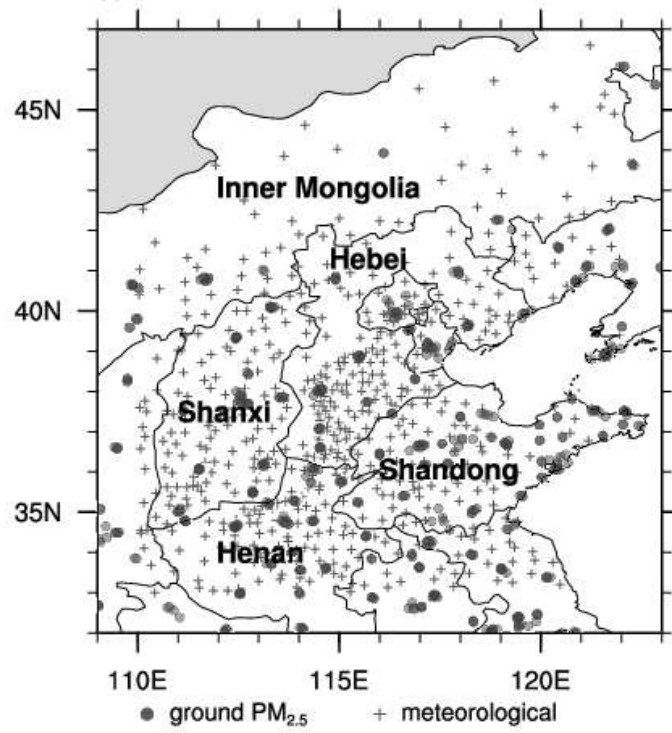


Figure 1. Ground PM_{2.5} observation sites (filled circles) and meteorological stations (gray crosses) over the NCP.

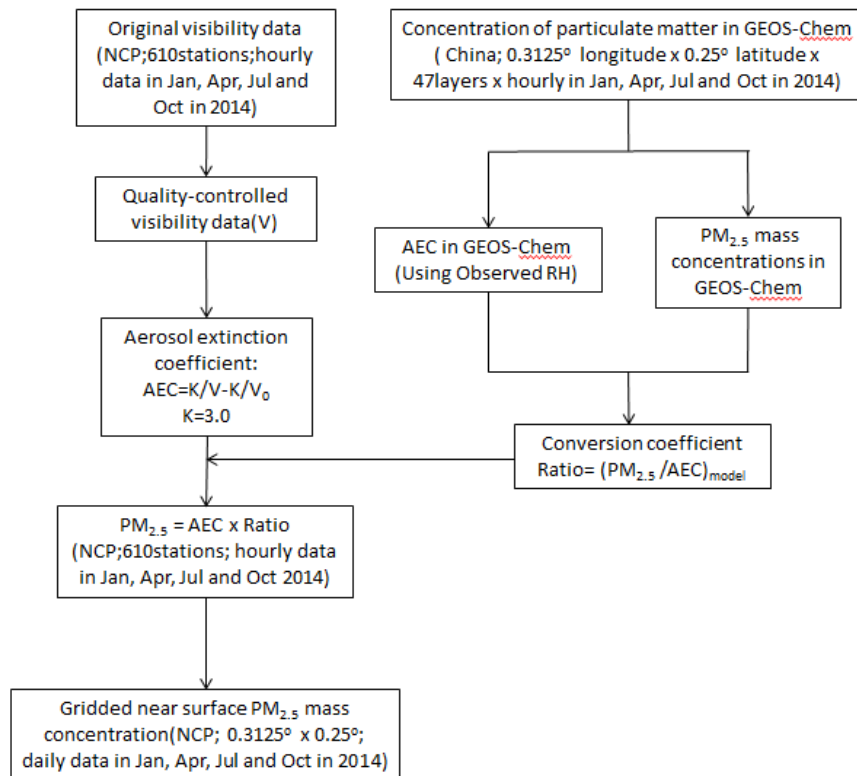


Figure 2. A flowchart for retrieval of gridded PM_{2.5} mass concentration data using visibility measurements and GEOS-Chem simulations. Data sources are shown in parentheses.

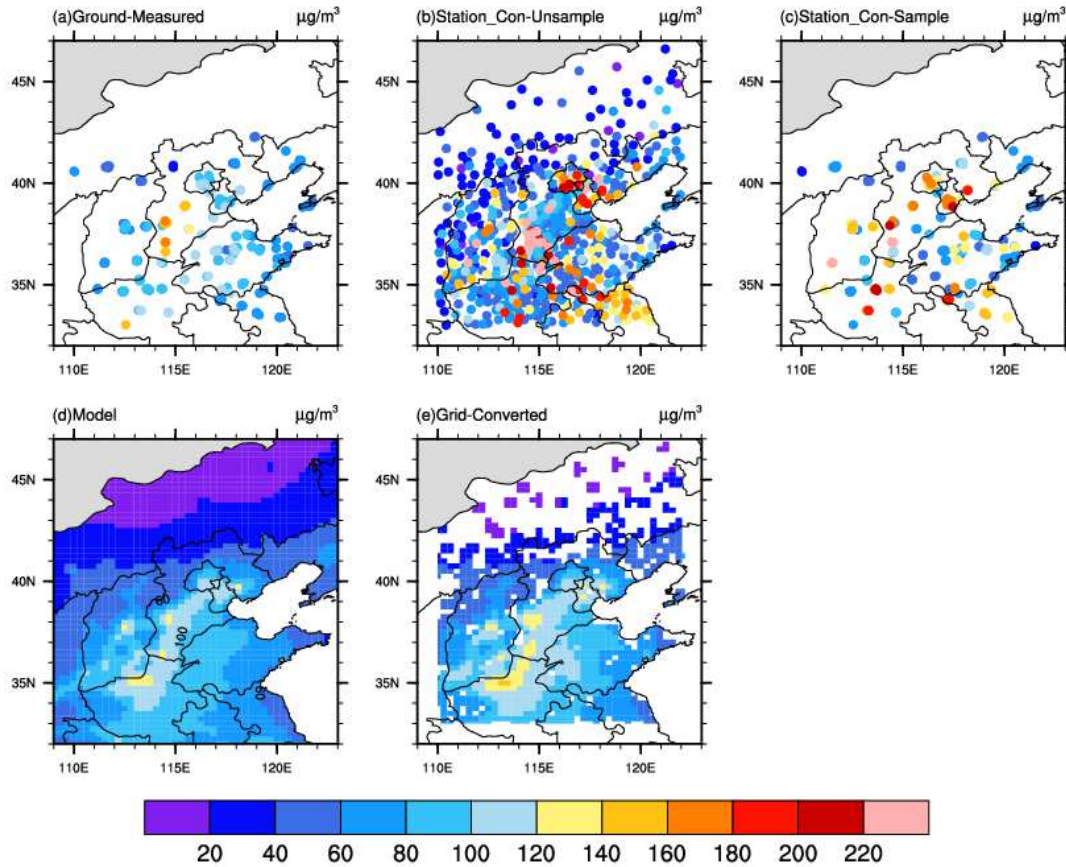


Figure 3. Spatial distributions of (a) observed (ground $\text{PM}_{2.5}$ observation sites), (b) Station-Converted (based on visibility measurement sites), (c) Station-Converted and sampled with observation times and locations (ground $\text{PM}_{2.5}$ observation stations), (d) modeled (simulated by GEOS-Chem), and (e) Grid-Converted (visibility-converted for grid cells under Case 7, with a radius of 0.3°) $\text{PM}_{2.5}$ concentrations averaged over January, April, July and October 2014. The black lines show provincial borders.

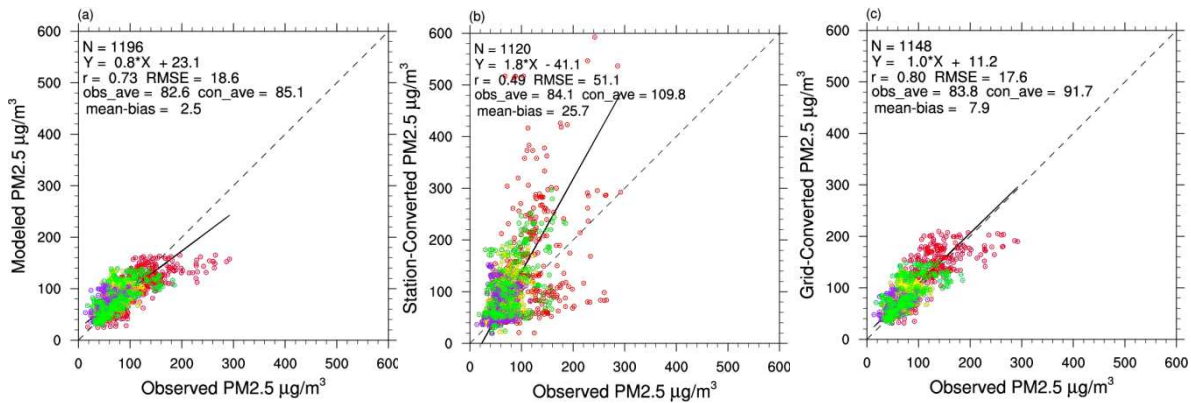


Figure 4. Scatter plots of (a) modeled, (b) Station-Converted and (c) Grid-Converted (Case 7, with a radius of 0.3°) PM_{2.5} (y-axis) with respect to PM_{2.5} observations (x-axis). A data point in the figure represents the monthly mean values (red-January, yellow-April, purple-July, green-October) at a station. The dotted line depicts the 1:1 relationship, and the solid line depicts the RMA regression line. Statistical analysis results are shown in each panel.

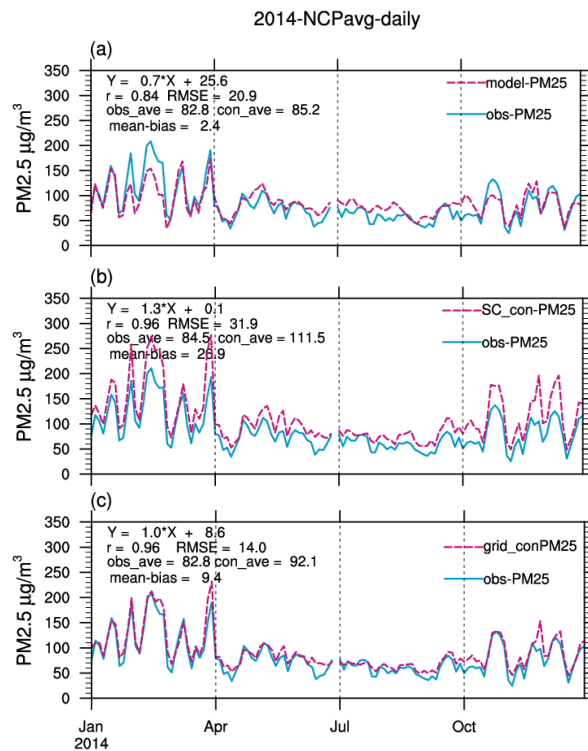


Figure 5. Day-to-day variation of (a) modeled, (b) Station-Converted and (c) Grid-Converted (Case 7, with a radius of 0.3°) $\text{PM}_{2.5}$ with respect to $\text{PM}_{2.5}$ observations in January, April, July and October 2014. For each day, $\text{PM}_{2.5}$ concentrations are averaged over all stations in the NCP. Statistical analysis results are presented in each panel. Modeled, Station-Converted and Grid-Converted data are sampled based on the observations.

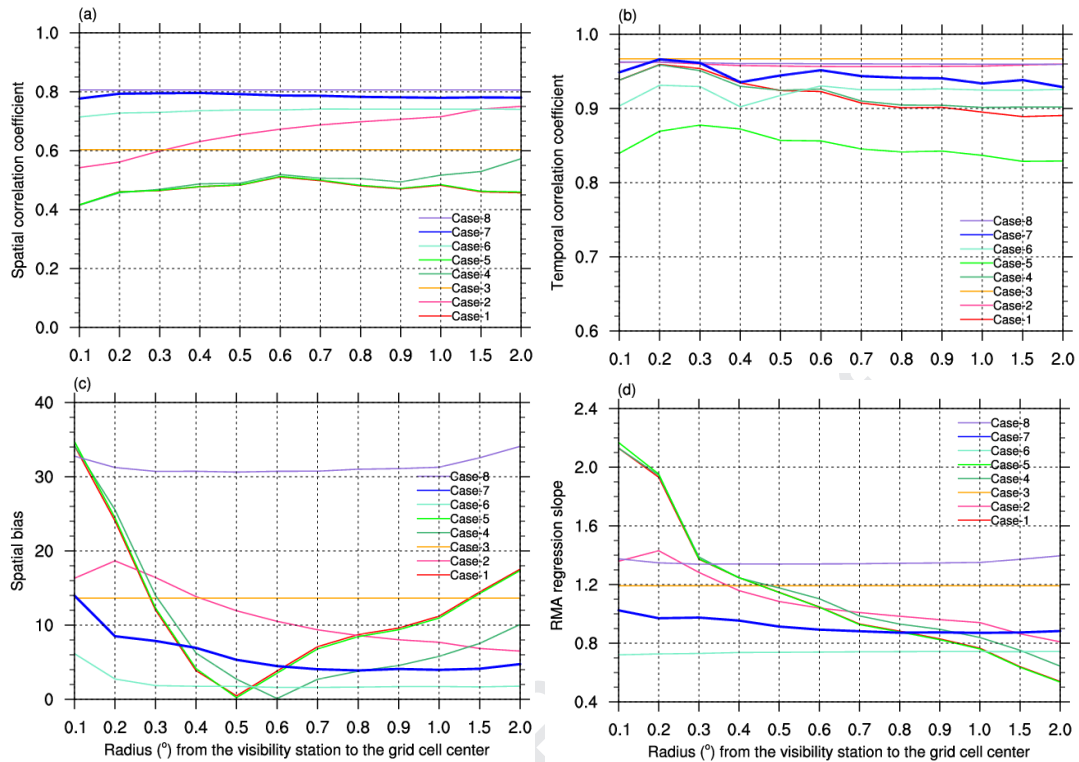


Figure 6. (a) Spatial correlation, (b) temporal correlation, (c) spatial bias (units: $\mu\text{g}/\text{m}^3$) and (d) linear regression slope (for spatial data) of Grid-Converted $\text{PM}_{2.5}$ concentrations with respect to $\text{PM}_{2.5}$ measurements in each station-to-grid conversion case, as a function of the distance (i.e., radius ranging from 0.1° to 2.0°) from the visibility station to the grid cell center.

Highlights

- We integrate visibility data and GEOS-Chem simulations to estimate $PM_{2.5}$ concentrations in 2014 over North China.
- Visibility converted $PM_{2.5}$ are spatiotemporally consistent with $PM_{2.5}$ measurements.
- Our method provides a novel, plausible way to retrieve long-term variation of $PM_{2.5}$.

The authors declare that they have no known competing financial interests or personal relationships that could have appeared to influence the work reported in this paper.

Journal Pre-proof